Atmos. Chem. Phys. Discuss., 13, 12389–12436, 2013
www.atmos-chem-phys-discuss.net/13/12389/2013/
doi:10.5194/acpd-13-12389-2013

Atmospheric Chemistry and Physics
Discussions
Open Access

Sulfur dioxide (SO_2) as observed by MIPAS/Envisat: temporal development and spatial distribution at 15–45 km altitude

M. Höpfner[1], N. Glatthor[1], U. Grabowski[1], S. Kellmann[1], M. Kiefer[1], A. Linden[1], J. Orphal[1], G. Stiller[1], T. von Clarmann[1], and B. Funke[2]

[1]Institute for Meteorology and Climate Research, Karlsruhe Institute of Technology, Karlsruhe, Germany
[2]Instituto de Astrofísica de Andalucía, CSIC, Granada, Spain

Received: 29 March 2013 – Accepted: 2 May 2013 – Published: 14 May 2013

Correspondence to: M. Höpfner (michael.hoepfner@kit.edu)

Published by Copernicus Publications on behalf of the European Geosciences Union.

Abstract

We present a climatology of monthly and 10° zonal mean profiles of sulfur dioxide (SO_2) volume mixing ratios (vmr) derived from MIPAS/Envisat measurements in the altitude range 15–45 km from July 2002 until April 2012. The vertical resolution varies from 3.5–4 km in the lower stratosphere up to 6–10 km at the upper end of the profiles with estimated total errors of 5–20 pptv for single profiles of SO_2. Comparisons with few available observations of SO_2 up to high altitudes from ATMOS, for a volcanically perturbed situations from ACE-FTS and, at the lowest altitudes, with stratospheric in-situ observations reveal general consistency of the datasets. The observations are the first empirical confirmation of features of the stratospheric SO_2 distribution which have only been shown by models up to now: (1) the local maximum of SO_2 at around 25–30 km altitude which is explained by the conversion of carbonyl sulfide (COS) as the precursor of the Junge layer, and (2) the downwelling of SO_2 rich air to altitudes of 25–30 km at high latitudes during winter and its subsequent depletion on availability of sunlight. This has been proposed as the reason for the sudden appearance of enhanced concentrations of condensation nuclei during Arctic and Antarctic spring. Further, the strong increase of SO_2 to values of 80–100 pptv in the upper stratosphere through photolysis of H_2SO_4 has been confirmed. Lower stratospheric variability of SO_2 could mainly be explained by volcanic activity and no hint for a strong anthropogenic influence has been found. Regression analysis revealed a QBO (quasi-biennial oscillation) signal of the SO_2 time series in the tropics at about 30–35 km, a SAO (semi-annual oscillation) signal at tropical and subtropical latitudes above 32 km and annual periodics predominantly at high latitudes. Further, the analysis indicates a correlation with the solar cycle in the tropics and southern subtropics above 30 km. Significant negative linear trends are found in the tropical lower stratosphere, probably due to reduced tropical volcanic activity and at southern mid-latitudes above 35 km. A positive trend is visible in the lower and middle stratosphere at polar to subtropical southern latitudes.

ACPD
13, 12389–12436, 2013

Stratospheric SO_2 by MIPAS

M. Höpfner et al.

1 Introduction

Sulfur dioxide (SO_2) is one of the key species determining the aerosol content of the stratosphere (SPARC, 2006). Main sources of stratospheric SO_2 are the conversion of carbonyl sulfide (COS) (Crutzen, 1976; Brühl et al., 2012) and the direct transport of SO_2 across the tropopause. This transport can occur abruptly through major volcanic eruptions or through upwelling predominantly at the tropical tropopause or through the monsoon circulation (Bourassa et al., 2012). However, there is still a lot of uncertainty regarding the major sources of stratospheric SO_2 during volcanically quiescent periods (Deshler et al., 2006; Hofmann et al., 2009; Vernier et al., 2011; Solomon et al., 2011; Brühl et al., 2012).

Loss of SO_2 occurs mainly through oxidation by OH radicals into H_2SO_4 vapour which condenses into liquid sulfate aerosols. Subsequently, sedimentation of particles results in a loss of sulfur from the stratosphere. Large-scale circulation leads to further upwelling of sulfur species in the tropical stratosphere where probably the photolysis of H_2SO_4 constitutes a further source of SO_2 (Rinsland et al., 1995; Vaida et al., 2003; Mills et al., 2005). During winter, downwelling of air in the polar vortices transports elevated amounts of SO_2 from the upper stratosphere down to altitudes of 30 km and below. Here, on availability of sunlight in spring, SO_2 is transformed through reaction with OH into H_2SO_4, thus leading to the formation of new particles. These processes have been proposed by Zhao et al. (1995) and Mills et al. (1999, 2005) as explanation for the sudden formation of enhanced layers of condensation nuclei (CN) in polar spring (Rosen and Hofmann, 1983; Hofmann and Rosen, 1985; Hofmann, 1990; Wilson et al., 1990). However, there has been no direct experimental evidence for this mechanism until now.

There exists a large dataset of SO_2 observations from space-borne nadir sounding instruments (e.g. Theys et al., 2012, and references therein). While these measurements have a good horizontal resolution, height-resolved profiles cannot be obtained (albeit some information on plume height has recently been derived, Van Gent et al., 2012; Carboni et al., 2012). Hence, measurements of the vertical distribution of SO_2 in the stratosphere are sparse. This is e.g. reflected in one of the recommendations within SPARC (2006, p. xii): "Observations of SO_2 in the upper troposphere and lower stratosphere and of H_2SO_4 and SO_2 in the middle and upper stratosphere would be extremely valuable to improve our modelling and predictive capabilities of stratospheric aerosol." Under volcanically perturbed situations enhanced mixing ratios of SO_2 facilitate their measurement. E.g. the SO_2 cloud from the eruption of Mt. Pinatubo in June 1991 has been analysed on basis of UARS-MLS observations by Read et al. (1993), and ACE-FTS measurements have been used to investigate SO_2 and sulphate aerosol from the Sarychev eruption in June 2009 (Doeringer et al., 2012).

Only three measured profiles of SO_2 covering the altitude range of the stratosphere have been published so far (Rinsland et al., 1995). In their work, on the basis of mean infrared solar occultation spectra during three space-borne flights of the ATMOS instrument, one SO_2 height profile per flight has been derived for the altitude range of about 30–50 km. The data revealed high concentrations of SO_2 in the upper stratosphere in the order of 100–400 pptv which was explained by photolysis of H_2SO_4. However, two of those profiles were strongly perturbed by the Pinatubo eruption and one possibly, but to a much less extent by El Chichón. Thus, there exists at most one observation of the background stratospheric SO_2 distribution.

In the present work we have analysed infrared limb-emission measurements by MIPAS/Envisat to obtain a global climatology of stratospheric SO_2 distributions from July 2002 until April 2012. First attempts on the retrieval of SO_2 from MIPAS have previously been performed by Burgess et al. (2005).

After an overview over the instrument (Sect. 2), the retrieval strategy and data characterisation will be described (Sect. 3). Then an overview of the dataset will be given in Sect. 4 followed by an assessment of its quality through comparison with independent observations and analysis of the internal variability (Sect. 5). In Sect. 6 the distribution of SO_2 will be discussed with respect to the various processes described above

ACPD
13, 12389–12436, 2013

including a regression analysis to single out correlations with external parameters, periodic cycles and trends.

2 Instrument

MIPAS (Michelson Interferometer for Passive Atmospheric Sounding) is one of the instruments on ESA's polar orbiting Envisat satellite (Fischer et al., 2008). Envisat was launched on 1 March 2002 and remained in operation until 8 April 2012 when contact was lost. With one major interrupt from April to December 2004, MIPAS measured quasi continuously from July 2002 until April 2012. The MIPAS FTIR (Fourier Transform Infra-Red) limb sounder recorded the radiation emitted by the Earth's atmosphere in the mid-infrared region with a spectral resolution of $0.025\,\mathrm{cm}^{-1}$ before April 2004 (period 1, P1) and $0.0625\,\mathrm{cm}^{-1}$ from January 2005 onwards (period 2, P2). MIPAS was operated alternately in different limb scan patterns. For this work we have used the most frequent "nominal" viewing modes. During P1 these consisted of 17 tangent altitudes (6–68 km with 3 km distances up to 42 km, followed by steps of 2×5 km and 2×8 km) which do not depend on the geographical position. During P2 the number of tangent views per limb-scan was increased to 27. Here tangent altitudes depend on latitude ranging from 5–70 km at the poles to 12–77 km over the equator with steps increasing with height from 1.5 km to 4.5 km. The horizontal distance between two subsequent limb scans in nominal measurement mode was around 550 km during P1 and 420 km during P2 resulting in about 1000 and 1400 limb-scans providing full latitudinal coverage per day.

3 Retrieval

Retrieval of SO_2 altitude profiles up to the middle stratosphere from MIPAS observations is difficult due to its small spectral signal relative to the spectral noise of MIPAS, especially under volcanically non-perturbed conditions. Therefore, we have chosen to

ACPD
13, 12389–12436, 2013

analyse monthly mean limb-spectra binned within 10° wide latitude bands. This method has already been employed for the detection of stratospheric $BrONO_2$ in Höpfner et al. (2009a).

In detail, first cloud-clearing has been performed on basis of the cloud-index (CI) method (Spang et al., 2004). This is necessary to avoid retrieval errors due to cloud/aerosol signal in the spectra. The CI is the spectral radiance contrast between two wavenumbers. A smaller CI indicates larger probability that the spectrum is contaminated by aerosols or clouds. We use a CI threshold of 4.5, i.e. spectra with CI < 4.5 are discarded. Further, all spectra in this limb sequence are discarded which were measured at lower tangent altitudes than that with CI < 4.5. Beside thick tropospheric clouds, this approach excludes e.g. also cirrus clouds, polar stratospheric clouds (Höpfner et al., 2009b) and optically thicker aerosol plumes from the subsequent analysis. Depending on atmospheric situation, particle composition and altitude, the applied CI limit equals a particle volume density of about 1–2 $\mu m^3 cm^{-3}$.

In the second step the limb-scans which are averaged within each latitude- and time-bin are selected. Here we have chosen those locations with the lowest available tangent altitude after cloud clearing under the condition that at least 300 limb-scans are averaged, which reduced the noise by a factor of at least 17. The noise reduction could be further improved by increasing the requested number of samples; this, however, would lead to loss of measurement points particularly at low altitudes and during months with sparser observational coverage. A decrease of the requested number of samples, on the other hand, would result in larger noise error contributions. For this analysis, MIPAS version 5 level-1b data have been used. Together with the averaged MIPAS spectra, for the retrieval mean pressure/temperature profiles are calculated from ECMWF analysis data at the position of each single limb scan. Further, mean tangent altitudes are obtained from the engineering MIPAS tangent altitude values. Errors resulting from these averaging processes are included in the error estimation as described further below.

The retrieval scheme is a constrained global fit approach using all tangent altitudes of one limb-scan with averaged spectra simultaneously (e.g., von Clarmann et al., 2003a):

$$\boldsymbol{x}_{i+1} = \boldsymbol{x}_i + \left(\mathbf{K}_i^T \mathbf{S}_y^{-1} \mathbf{K}_i + \mathbf{R}\right)^{-1} \times \left[\mathbf{K}_i^T \mathbf{S}_y^{-1} (\boldsymbol{y}_{\text{meas}} - \boldsymbol{y}(\boldsymbol{x}_i)) - \mathbf{R}(\boldsymbol{x}_i - \boldsymbol{x}_\text{a})\right] \tag{1}$$

which is a variant of the formulation suggested by Rodgers (2000). Here, $\boldsymbol{x}$ is the vector containing the atmospheric and instrumental parameters to be determined. The atmospheric profiles are gridded at 1 km altitude levels in-between which the volume mixing ratios (vmr) vary linearly with height. $\boldsymbol{y}_\text{meas}$ are the averaged measured radiances of all tangent altitudes and $\mathbf{S}_y$ is the measurement noise covariance matrix. $\boldsymbol{y}_i$ contains the spectral radiances which are simulated with the radiative transfer model KOPRA (Stiller, 2000) using the results obtained in iteration number i. $\mathbf{K}_i$ is the Jacobian matrix, i.e. the partial derivatives $\partial \boldsymbol{y}(\boldsymbol{x}_i)/\partial \boldsymbol{x}_i$ determined in parallel to $\boldsymbol{y}_i$ at each iteration step. $\boldsymbol{x}_\text{a}$ contains the a-priori profiles. For the target species SO_2, altitude-constant initial guess and a-priori profiles, $\boldsymbol{x}_0$ and $\boldsymbol{x}_\text{a}$ equal 10 pptv, have been used whereas for all other trace gases climatological values have been chosen.

For the regularisation matrix $\mathbf{R}$ a first-order smoothing constraint $\mathbf{R} = \gamma \mathbf{L}^T \mathbf{L}$, where $\mathbf{L}$ is a first order finite differences operator (Tikhonov, 1963; Steck, 2002) has been used in order not to bias the retrieval results. Thus, the choice of the altitude-constant a-priori value for SO_2 has no influence on the resulting profiles. The regularization parameter γ depends only on the species but not on the altitude. It was chosen such to avoid instabilities showing up as oscillations in the retrieved atmospheric profiles.

Line-by-line calculations have been based on the HITRAN 2008 compilation including updates until 2010 (Rothman et al., 2009). The spectral intervals (microwindows) used for the retrieval are located in the same wavenumber region ($\sim$ 1366–1377 cm^{-1}) within the SO_2 ν_3-band as those selected for the analysis of ACE-FTS (Doeringer et al., 2012) and of ATMOS data (Rinsland et al., 1995). In detail, we have chosen the four microwindows 1366.575–1367.925 cm^{-1}, 1369.95–1370.375 cm^{-1}, 1371.2–1371.925 cm^{-1}, and 1376.0–1376.375 cm^{-1} in case of the high-spectral resolution mode of MIPAS (P1) and 1366.5625–1367.9375 cm^{-1}, 1369.9375–1370.375 cm^{-1},

ACPD
13, 12389–12436, 2013

1371.1875–$1371.9375\,cm^{-1}$, and 1376.0–$1376.375\,cm^{-1}$ for the measurements during P2. These have been selected to gain a good sensitivity for SO_2 while avoiding the strongly interfering spectral signatures of other gases as far as possible. To further minimize these interferences the following gases have been jointly retrieved with SO_2: H_2O (isotopologues: $H_2^{16}O$, HDO, $H_2^{18}O$), CO_2, O_3, CH_4, HCN and HO_2. Further, instrumental parameters which have been included in the parameter vector $\boldsymbol{x}$ are a spectral shift correction per microwindow and an additive calibration offset per microwindow and tangent altitude. No regularisation has been applied in case of these instrumental quantities.

Figure 1 presents an example of the spectral fit achieved in all four microwindows for MIPAS measurements with higher (top 3 rows) and lower spectral resolution (bottom 3 rows). Spectral residuals between measurements and simulation are shown for the case where no SO_2 has been retrieved (2nd and 5th row) and under consideration of SO_2 (3rd and 6th row). It is obvious that in both cases, the fit residual is strongly improved by including SO_2 into the fit parameter vector, and that the residuals without SO_2 fit (black lines in 2nd and 5th row) are mostly produced by SO_2 spectral signatures (green lines in 2nd and 5th row).

For characterisation of the vertical resolution of the retrieval the related averaging kernels have been determined as

$$\mathbf{A} = \left(\mathbf{K}^T\mathbf{S}_y^{-1}\mathbf{K} + \mathbf{R}\right)^{-1}\mathbf{K}^T\mathbf{S}_y^{-1}\mathbf{K}. \qquad (2)$$

The rows of $\mathbf{A}$ represent the contributions of different altitudes to the retrieved vmr profile of SO_2 whereas the columns are the responses of the system to a delta function at the associated altitude. Typical averaging kernels are shown in Fig. 2 for period P1 (top) and P2 (bottom). The overall diagonal structures of $\mathbf{A}$ demonstrate that the retrieval of SO_2 behaves well with better vertical resolution at lower compared to higher altitudes due to the better sensitivity (higher pressure) and a denser tangent altitude sampling there. Typical values for the vertical resolution as derived from the width of the columns of **A** and from the inverse of the diagonal of **A** in both measurement modes vary around 3.5–4 km at 20 km, 4–5 km at 30 km and 6–10 km at 40 km altitude.

An estimate of the altitude dependent errors is presented in Fig. 3. Typical mean error profiles calculated for one month (January 2003) of period P1 and one month (January 2011) of P2 are shown together with the single error contributions which are combined to the total error by calculating the root sum squared of the single terms.

The following sources of uncertainty have been taken into account: spectroscopic errors of SO_2 line-intensity (spe_int_SO2) and air-broadened half-width (spe_hw_SO2). For the line-intensity an uncertainty of 5 % and for the half-width 15 % has been assumed. Both values are on the conservative side of the errors stated in Rothman et al. (2009). The spectroscopy of interfering trace gas signatures has been handled as an independent error source by assigning also here errors of line-intensity (spe_int_itf) and half-width (spe_hw_itf) of 5 % and 15 %, respectively. Major instrumental uncertainties are estimated as 1 % for gain calibration (gain), 3 % for the instrument line shape (ils) (in terms of linear loss of modulation efficiency toward the maximum optical path difference of the interferometer) and 300 m for tangent altitude pointing (htang). Spectral noise (noise) is based on the actual level 1b dataset as delivered together with the calibrated spectra. For the uncertainty of ECMWF temperatures (Tecm) values of 2 K below and 5 K above 35 km altitude are assumed. A further error term which has to be taken into account for retrievals from averaged spectra is the effect of retrieval non-linearity (nlin). This error contribution is estimated on basis of dedicated retrieval simulations as described in detail in Höpfner et al. (2009a) except that the values used for the line-of-sight uncertainty of single observations have been 400 m for the P1- and 300 m for the datasets during P2. These values have been determined from comparison of engineering tangent altitude values with those obtained by the pointing retrievals during the standard IMK/IAA data analysis (von Clarmann et al., 2003b, 2009; Kiefer et al., 2007).

4 Dataset overview

Figures 4–6 present an overview of all MIPAS results of SO_2 as color-coded cross-sections versus time. As mentioned above, the lower altitude limit of the dataset is defined by the condition on the minimum number of limb-scans used to calculate mean spectra. This is determined by (a) the cloud coverage, (b) the scan-pattern of MIPAS and (c) the lower limit of 15 km set to confine the retrievals mainly on the stratospheric situation. The influence of clouds can best be seen at the data gaps during the Antarctic winter season where the MIPAS observations are obscured by Polar Stratospheric Clouds (e.g. top row in Fig. 4). High clouds also restrict some of the observations at low altitudes in tropical regions during P1 until March 2004. Further data-gaps covering the whole altitude region are present in 2005 and 2006 when MIPAS measurements were still sparse during the first years in the new operational mode.

As basis for subsequent discussions the dataset has been reduced by averaging to the mean profiles for four seasons and 8 latitude regions (see Fig. 7, top two rows). These profiles represent background situations since volcanically strongly perturbed periods, as detailed in the caption of Fig. 7 have been neglected during averaging. The related variability is described in the bottom two rows of Fig. 7 by the altitude-dependent standard deviation.

5 Data quality

Here we assess the quality of the MIPAS SO_2 dataset by comparison with independent measurements. Further the estimation of random errors will be validated by comparison to the variability derived from the dataset itself.

5.1 Comparison with ATMOS

The only measurements of SO_2 reaching up to the upper stratosphere so far were published by Rinsland et al. (1995). These three profiles are compared with MIPAS data

ACPD
13, 12389–12436, 2013

obtained for similar latitudes and months in Fig. 8. The ATMOS profile of 1992 and, to a lesser extent, also that of 1993, are influenced by the eruption of Mt. Pinatubo in June 1991 (Rinsland et al., 1995). Thus, the one which can best be compared to the MIPAS dataset is the ATMOS mean profile of 1985. Mind that this has also been observed under enhanced stratospheric aerosol levels due to the eruption of El Chichón in March 1982, albeit to a less extend than ATMOS 1991 and 1993 (SPARC, 2006, e.g. Fig. 4.35).

Throughout the altitude range between 33 and 45 km, the MIPAS mean profile is within the uncertainty range of ATMOS 1985. Only at the lowest 2 km MIPAS mean volume mixing ratios of SO_2 are larger than ATMOS by about 20 pptv. However, accounting for the variability, the MIPAS profiles are comparable to those of ATMOS at these altitudes. MIPAS agrees with both post-Pinatubo ATMOS measurements up to altitudes of 32 and 35 km, respectively. Above these heights ATMOS shows strongly increasing concentrations up to values of 400 pptv compared to maximum MIPAS values of 100 pptv. The fact that at lower altitudes around 30 km the values of SO_2 do not deviate from MIPAS as strongly as above 35 km even for volcanically enhanced conditions can most probably be explained with the major part of sulfur being in the form of H_2SO_4 at those altitudes.

5.2 Comparison with ACE-FTS

A direct comparison with observations by ACE-FTS is possible for a volcanically enhanced situation directly after the Sarychev eruption in June 2009. In Fig. 8 of their paper Doeringer et al. (2012) present the measured zonal mean distribution of SO_2 between 12 and 20 km for the first half of July 2009. This can be compared to the MIPAS monthly mean distribution as shown in Fig. 9. At the lowest comparable level of 15 km ACE-FTS values are around 540–620 pptv between 50° N and 70° N. In this latitude range, MIPAS volume mixing ratios are about 420 pptv. At the same geographical latitudes and 17 km altitude MIPAS values are 130–170 pptv versus about 330 pptv in case of ACE-FTS, and at 40° N MIPAS observed 210 pptv while ACE-FTS reported

ACPD
13, 12389–12436, 2013

around 270 pptv. Further, the decrease in altitude of the volcanically SO_2-enhanced air masses towards north is similar for both datasets. Regarding the locally and temporally sparse coverage of ACE-FTS (see the lower panel of Fig. 9 in Doeringer et al., 2012) compared to MIPAS the observed differences do not hint at a problem in the MIPAS dataset of SO_2 during volcanically perturbed situations.

5.3 Comparison with in-situ observations

In-situ measurements of SO_2 at comparable altitudes to those presented here for the mean MIPAS profiles are extremely sparse since they have mainly been obtained from aircraft up to the lowermost stratosphere. Table 1 shows a selection of published in-situ datasets in which explicitly stratospheric values have been indicated which can best be compared to the mean profiles as shown in Fig. 7. The only in-situ dataset reaching into the altitude range presented here is the one obtained by Inn and Vedder (1981) up to an altitude of 20.4 km in June/July 1979. The reported values of 36–50 pptv at 15 km are higher (or at the upper end when taking into account the reported error of 50 % of the in-situ data) compared to the MIPAS average background vmr-distribution (around 13 ± 10 pptv) at mid-latitudes (cf. Fig. 7). At around 20 km reported SO_2 mixing ratios of 45 and 51 pptv (±50 %) at 64° N and 67° N are clearly much higher than MIPAS mean values which are around 6 pptv. Even under perturbed situations like the eruption of Sarychev, MIPAS monthly mean data at around 20 km altitude and similar latitudes are less than 20 pptv. Thus, either the aircraft data has been obtained within a locally perturbed situation not representative for the mean background or the difference points to problems of either the in-situ data or the MIPAS analysis.

Other observations reaching nearly the lower limit of the altitude range of our MIPAS dataset are the first measurements of SO_2 by Jaeschke et al. (1976) at 14 km and various stratospheric data by Meixner (1984), both obtained in northern mid-latitudes. Comparing the data in Fig. 7 at the lower end of the profiles with those observations shows that MIPAS mean values are generally at the lower part of the variability of the in-situ data. However, when considering the generally increasing MIPAS data at

ACPD
13, 12389–12436, 2013

northern mid-latitudes with decreasing altitude is seems reasonable that the typically higher in-situ data at lower heights might be compatible. Since the other stratospheric data listed in Table 1 are similar to those already discussed, we conclude that in general the MIPAS values at the bottom end of their altitude range are at the lower limit of in-situ observations.

5.4 Internal variability

As described in Sect. 3 the instrument noise dominates the error characteristics over a large part of the profile. We have tried to validate this error term by comparing it to the temporal month-to-month variability of the retrieved SO_2 profiles at distinct altitudes for the different latitude bins. This method is similar to the one used for validation of the precision of MIPAS single-scan data products (Piccolo and Dudhia, 2007). Figure 10 shows for each latitude l and altitude h the standard deviation $\Delta\delta_{l,h}$ of the noise-error ($\epsilon_{l,h,m}$) weighted difference $\delta_{l,h,m}$ of the SO_2 volume mixing ratios $x_{l,h,m}$ between subsequent months m where M is the number of months:

$$\Delta\delta_{l,h} = \left(\frac{1}{M-2} \sum_{m=1}^{M-1} \left(\delta_{l,h,m} - \bar{\delta}_{l,h}\right)^2 \right)^{\frac{1}{2}} \tag{3}$$

with

$$\delta_{l,h,m} = \frac{x_{l,h,m} - x_{l,h,m+1}}{\sqrt{\epsilon^2_{l,h,m} + \epsilon^2_{l,h,m+1}}}, \tag{4}$$

where ϵ is the estimated error due to instrument spectral noise. In the ideal case $\Delta\delta_{l,h}$ would be equal 1. Values greater than 1 indicate either that the natural variability of SO_2 from month to month is not negligible (thus increasing the numerator of Eq. 4) or the noise errors are underestimated (denominator of Eq. 4). In Fig. 10 enhanced values of $\Delta\delta_{l,h}$ in the northern and equatorial lower stratosphere and at all altitudes in high-latitude regions are very likely due to the natural variability caused by volcanic activity and the downwelling of SO_2-rich air into the polar vortices during winter. Anthropogenic influence might be a further source for the enhancements at northern latitudes. Excluding those regions, i.e. for 50° S–50° N and altitudes ≥ 30 km the mean value of $\Delta\delta_{l,h} = 1.5 \pm 0.1$. Thus, it can be concluded that the estimated noise error may underestimate the instrumental random error by no more than 50 %. The difference between estimated noise and month-to-month variability may be explained by either natural variability or by random parts of the total error estimation like variations in the gain-calibration or the ECMWF temperature/pressure dataset which are not included in the pure spectral noise error.

6 Results and discussion

6.1 Mid-stratospheric maximum

The main chemical production of SO_2 in the stratosphere appears via conversion from COS leading to a local maximum of SO_2 in the mid-stratosphere (Crutzen, 1976; Brühl et al., 2012). The MIPAS observation show this maximum very pronounced in the tropics as visible in Figs. 4 and 5 at altitudes of around 27–30 km. The mean latitudinal and seasonal variation of this maximum can better be inspected in averaged stratospheric background profiles as presented in Fig. 7. For calculation of these profiles major volcanically perturbed seasons (for details see caption of Fig. 7) have been excluded. In the tropics, the mid-stratospheric maximum of the mean profiles is located at 28–30 km decreasing in altitude towards the poles down to 25 km in the northern and 23 km in the southern summer months. In the tropics, the vmr value of the maximum varies around 40–50 ppt. Towards higher latitudes summertime values decrease towards 20 pptv at subtropics, 10 pptv at middle- and 5 pptv at polar latitudes. During other seasons the maximum is less discernible from the generally increasing values towards higher altitudes.

ACPD
13, 12389–12436, 2013

The tropical MIPAS values can be compared with model results shown in Fig. 6 of Brühl et al. (2012). Here the altitude of the maximum varies around 28–31 km, depending on time between 1999 and 2002. In this time range the vmr values vary around 30–60 pptv which is similar to the temporal variability of our observations as shown in Fig. 4 and 5.

The local maximum in MIPAS mean profiles of SO_2 (Fig. 7) can further be compared with the results of five different models as shown in SPARC (2006, Fig. 6.11) (http://www.sparc-climate.org/publications/sparc-reports/sparc-report-no4/) and Fig. 6.2 of its supplement to Chapter 6. In these simulations the altitude of the tropical maximum is located between 29 and 32 km. The maximum vmr values of 40–50 pptv for four models compare well with MIPAS while the ULAQ model is with about 20 pptv considerably lower. At 45° latitude in July the models indicate lower maximum altitudes of 24–27 km in accordance with MIPAS. The model vmr varies here between 8 and 20 pptv which is comparable to the MIPAS variation between mid-latitude and sub-tropical mean profile maximum values of 10–20 pptv.

6.2 Enhanced upper stratospheric values and polar downward transport

In the tropics, the production of SO_2 from COS fades out shortly above 30 km due to the unavailability of COS leading to a decrease of the SO_2 mixing ratio (Brühl et al., 2012). Above about 33 km our measurements show again an increase of SO_2 volume mixing ratios reaching average values of about 80–100 pptv (Fig. 7) at 45 km. At these altitudes, the SO_2 concentrations do not show any large variability with latitude. This increase of SO_2 from the middle to the upper stratosphere is caused by photolysis of H_2SO_4 which is released due to the evaporation of aerosols (Vaida et al., 2003; Mills et al., 2005). At altitudes of 45 km Brühl et al. (2012, Fig. 6) show values of around 50 pptv of SO_x (mostly SO_2) being considerably smaller than our data. This can be explained by neglecting in the model SO_2 photolysis bands in the visible and near-IR (Brühl et al., 2013). The models in SPARC (2006, Fig. 6.11) show large differences at these altitudes: in the tropics three of the models underestimate the observed SO_2

ACPD
13, 12389–12436, 2013

values above the mid-stratospheric maximum, while the LASP model compares rather well. However, at 45° N this model overestimates the high-altitude MIPAS observations by a factor of 2 while other models are still lower than the observations.

In wintertime at high latitudes the MIPAS data show the descent of enhanced upper stratospheric SO_2 concentrations down to 20–25 km altitude (blue curves in Fig. 7). On average at 30 km vmr values of 50–60 pptv and at 25 km 20–40 pptv are reached. This periodic effect is clearly visible in the top rows of Figs. 4 and 5. The mean evolution over the Antarctic from July to December is shown in detail in Fig. 11 which can be compared with the simulations shown in Mills et al. (2005, Fig. 5). In those model runs highest SO_2 values of about 100 pptv at 30 km and 60 pptv at 25 km altitude are reached in the Antarctic polar vortex by end of August. In the observations, highest SO_2 concentrations at these altitudes are observed in July/August with mean values of up to 60 pptv at 30 km and 40 pptv at 25 km altitude (see Fig. 11). In September/October the model shows a sudden decrease of SO_2 concentrations through photolysis leading to the production of small aerosol particles. This behaviour is well reflected in the MIPAS dataset (cf. Fig. 11) where a first decrease is visible below 30 km altitude between August and September followed by a stronger decrease between September and October below about 35 km.

6.3 Lower stratospheric variability

In Fig. 6 we have indicated the time and geographical latitude of major volcanic eruptions by orange triangles together with the initials of each volcano as specified in Table 2. As basis for this list we have taken the one compiled by Neely et al. (2013) and added further eruptions being visible in the MIPAS dataset. For that purpose, the retrieval of SO_2 from single MIPAS observations (which is the topic of a separate study to be published) has been used to unambiguously assign elevated amounts of SO_2 to volcanic events. The clear correlation of volcanic eruptions with elevated values of SO_2 in the top four rows of Fig. 6 shows that the major variability of SO_2 in the altitude range below about 22 km is determined by volcanic activity.

In the first half of the MIPAS measurement period, until end of 2006, equatorial volcanic eruptions dominate the SO_2 mean distribution in the lower stratosphere near the equator (cf. Figs. 4 and 5) while during the second part mid- and high northern latitudes are mostly affected. Figure 12 compares the temporal evolution of the global SO_2 content derived from MIPAS for the altitude regions 15–23 km and 20–23 km with the total injected mass as derived from nadir sounding instruments (cf. Table 2). In case of the larger eruptions of Kasatochi, Sarychev and Nabro, the mean SO_2 content at 15–23 km in the month directly after the eruption is about 1–2 % of the total injected mass. As shown in Sect. 5.2, due to the similar distribution of SO_2 volume mixing ratios between ACE-FTS and MIPAS after the eruption of Sarychev (Doeringer et al., 2012), also the total mass derived from both instruments would be comparable.

For tropical eruptions, like those of Soufrière Hills, El Reventador or Raboul, the SO_2 mass in the lower stratosphere is in the order of 5 % or more of the total mass, likely due to the general upward transport in the tropical UTLS region. As already indicated in the plots of volume mixing ratio, the lower panel of Fig. 12 shows that altitudes above 20 km are mainly affected by the tropical eruptions before end of 2006. Roughly about 2 % of the listed total SO_2 mass of tropical volcanoes seem to reach these high altitudes while this is only about 0.1 % in case of large mid-latitude eruptions. Mind (1) that the MIPAS values of SO_2 mass in 2005 and 2006 are underestimated due to the sparser coverage compared to earlier and later dates as indicated by the red crosses in Fig. 12 and (2) that due to the cloud threshold described in Sect. 3, strongly aerosol contaminated limb-views are excluded from the retrieval leading to a general underestimation of SO_2. The latter effect, however, only affects few limb-scans directly after the eruption in the vicinity of the major plume such that the monthly mean values are unlikely to be disturbed.

The SO_2 distributions within the tropical regions in Figs. 4 and 5 can be inspected for indications of upward transport of SO_2 from the periods of volcanically enhanced values in the lower stratosphere up to the SO_2 maximum at around 28 km. After the three major tropical events in the period until 2007 (end 2002, begin 2005 and mid

2006) an upwelling of SO_2-enhanced air is tentatively visible. However, due to the processing of SO_2 during the months directly after the eruptions much smaller values of SO_2 remain for an upward transport. It is merely probable that sulfur is transported in the form of aerosols as has been shown e.g. in Vernier et al. (2011, Fig. 2). The time series of SO_2 show that enhanced values at its mid-stratospheric maximum near 28 km and above are present some months after the eruptions. However, as described in the following chapter there is a strong correlation with the quasi-biennial oscillation (QBO) especially at those altitudes. The resulting maxima of SO_2 are superposed to possible enhancements due to the volcanic eruptions and, thus, both effects are difficult to disentangle.

6.4 Regression analysis

In this section, the temporal development of the SO_2 dataset is analysed under consideration of a constant term a, a linear term b, several periodics and external parameters with coefficients c, d, and e using a multivariate fit approach as proposed by von Clarmann et al. (2010) and extended by Stiller et al. (2012). A regression function vmr(t) is fitted to the time series of SO_2 values at each 2 km altitude and 10° latitude bin:

$$\begin{aligned}\mathrm{vmr}(t) &= a + bt + c_1 \mathrm{qbo}_1(t) + d_1 \mathrm{qbo}_2(t) \\ &\quad + c_2 \sin\frac{2\pi t}{T_1} + d_2 \cos\frac{2\pi t}{T_1} \\ &\quad + c_3 \sin\frac{2\pi t}{T_{0.5}} + d_3 \cos\frac{2\pi t}{T_{0.5}} \\ &\quad + eF_{10.7}(t).\end{aligned} \tag{5}$$

Here $\mathrm{qbo}_1(t)$ and $\mathrm{qbo}_2(t)$ are the Singapore time series of winds at 10 hPa and 50 hPa as provided by the Free University of Berlin (http://www.geo.fu-berlin.de/en/met/ag/strat/produkte/qbo/index.html). They are used to describe the QBO signal in the time series (Kyrölä et al., 2010). The sine and cosine terms describe annual

($T_1 = 1$ yr) and semi-annual ($T_{0.5} = 0.5$ yr) variability including a phase-shift. The solar radio flux at 10.7 cm ($F_{10.7}(t)$) provided by the NOAA Space Weather Prediction Center (http://www.swpc.noaa.gov), serves as proxy for solar activity (Kyrölä et al., 2010). A possible offset between P1 and P2 data is accounted for by adding a fully correlated block matrix to the P1-part of the data error covariance matrix.

In Fig. 13 results of the regression analysis are shown for exemplary latitude/height bins illustrating the influence of various partial signals. In the following this Fig. 13 is discussed together with Fig. 14 where the global distribution of the amplitudes of the single regression functions is presented (see caption of Fig. 14 for a more detailed description).

The quality of the fit is illustrated by the χ^2 of the regression (see plot "CHI2" in Fig. 14). In general the global fit quality is relatively homogeneous. Main exceptions are the regions of the polar upper stratosphere and the northern lowermost stratosphere with higher values of χ^2. The latter is probably explained by volcanic activity the influence of which was mainly concentrated at altitudes up to 20 km in the north (see Sect. 6.3). Further, influences by anthropogenic sources may also contribute to the higher values of χ^2 there. Enhanced χ^2 at high latitudes above 30–35 km altitude stem from strongly increased values of SO_2 up to 120–160 pptv during single winter months (see e.g. top row of Fig. 5) which cannot be represented adequately by the regression model.

The QBO signal can clearly be detected in the tropics at altitudes of 28–36 km introducing a variability in SO_2 of around ±20 pptv (cf. top right panel in Fig. 14 and example "QBO" in Fig. 13). Here the major part of the QBO signal stems from $\text{qbo}_1(t)$, the Singapore winds at 10 hPa whereas the winds at 50 hPa ($\text{qbo}_2(t)$) are of minor importance. High values of SO_2 are correlated with the easterly phase of the QBO. Such a QBO signal has also been observed in case of time series of stratospheric aerosol extinction (Trepte and Hitchman, 1992; Vernier et al., 2011).

Large amplitudes (up to about 30 pptv) of the annual modes are present especially at altitudes of 25–35 km at polar latitudes (cf. Fig. 14). These are explained by the

ACPD
13, 12389–12436, 2013

downwelling of SO_2-rich air from higher altitudes during winter. The N–S asymmetry with larger amplitudes at lower altitudes in the south are presumably due to the more persistent Antarctic polar vortex.

The mode of the semi-annual oscillation (SAO) with amplitudes of up to 10 pptv of SO_2 is visible above 30 km altitude at tropical and subtropical latitudes (Fig. 14). This mode can be identified in the example dataset for 20–30° S at 41–43 km altitude (see panel "Semi-Annual" in Fig. 13) by a second, smaller peak in the second half of each year. Such a seasonal asymmetry with stronger variation during the first cycle has been described as typical feature of the equatorial SAO (Delisi and Dunkerton, 1988; Garcia et al., 1997). Further, a latitudinal asymmetry of the SAO with stronger intensity southwards of the equator as indicated in Fig. 14 has been observed previously in observations of temperature and wind (Belmont and Dartt, 1973; Ray et al., 1998). The global distribution of the reconstructed linear slope is presented in Fig. 14 (bottom, right). It shows generally a slight positive trend at all altitudes in the northern and, with larger values, below about 32 km in the southern extra-tropical latitudes. Negative trends are mainly visible at higher altitudes in the southern sub-tropics and mid-latitudes and at lower altitudes in the tropics. Single examples for times series indicating stronger positive and negative trends at different altitudes in the southern mid-latitudes are shown in Fig. 13. Here at 25–27 km altitude a positive trend is visible for the whole dataset and even when considering only data after e.g. 2007. At 41–43 km the data show a general decrease until about 2009 and a levelling off afterwards. As discussed above, this correlates also with the $F_{10.7}$ flux time series and it might be that part of the solar variability is mapped into the linear slope (and vice versa). In fact, in Fig. 14 the upper atmospheric part with negative linear slope in the south is correlated with the area of strongest $F_{10.7}$ amplitude. To determine more specifically the significance of the trend values we have used the method of model-error correction as described in detail in Stiller et al. (2012, Sect. 7). In short, the error covariance matrix of the data is inflated and mean error correlations are inferred from the fit residuals such as to achieve a unity χ^2 of the fitted trend residuals. This increased error accounts for deficiencies in the linear regression to describe the real atmospheric situation and any underestimation of the measurement errors. The results of this analysis are presented in Fig. 15. The corrected values of the slope are very similar to the ones determined originally under the assumption of measurement error only. The corresponding significance of the slope in terms of its error σ is shown in the middle left of Fig. 15 and in the bottom left part the remaining data points for which the trend is larger than 2σ are presented. The latter clearly shows that the only larger contiguous area of significant positive trend is located in the Southern Hemisphere reaching from 25–30 km in the subtropics down to the lower stratosphere in polar regions. This area separates two regions of negative slope: one above 35 km at austral mid-latitudes, the other in the tropical stratosphere below 25 km. Single time series of the latter (cf. Fig. 13 right, bottom) strongly suggest that the negative slope is caused by larger tropical volcanic influence at the beginning of the first and of the second MIPAS measurement period compared to the end of both periods.

A connection with solar activity is indicated by a maximum signal of about 20 pptv for the fit with the $F_{10.7}$ cm flux at mostly tropical and sub-tropical latitudes above 30–35 km altitude (cf. Fig. 14). This correlation stems from a positive curvature of the 10 yr dataset as visible in panel "$F_{10.7}$" of Fig. 13. Mind, however, that there is a correlation between the long-wave $F_{10.7}$ time series, a linear trend and the independent bias values of the first and the second MIPAS measurement period. E.g., if SO_2 vmr values of the first period had a systematic positive offset compared to the second period, the $F_{10.7}$ index would partly compensate for it. However, inspection of single time series (like in Fig. 13) reveals that increases after 2010 from a lower constant level during the years 2007–2010 are present in the data sets of the second period, which is in correspondence with the solar cycle. As for the linear trend just described, we have estimated the significance of the solar cycle signal as shown in the right part of Fig. 15. Here the major contiguous area of significant $F_{10.7}$ signal is located in the mid to upper tropical stratosphere.

ACPD
13, 12389–12436, 2013

7 Conclusions

We have retrieved zonal 10° mean stratospheric distributions of SO_2 from MIPAS/Envisat monthly mean spectra for the period 2002–2012. These are the first observations of height-resolved SO_2 covering (1) nearly the entire region of the stratosphere, (2) the whole globe, and, (3) a time period of about 10 yr. Retrieval diagnostics indicate total error bars of 5–20 pptv most of which is dominated by instrumental noise followed by non-linearity uncertainties due to the retrieval approach at lower altitudes and assumptions on temperature at higher levels. Since the a-priori profiles of the retrieval has been chosen constantly zero over the whole altitude range, the shape (apart from some smoothing due to the regularisation type) and the absolute values of the retrieved profiles are entirely based on information from the measurements.

The lack of stratospheric SO_2 observations poses a problem for validation of our dataset. To get an estimate on the data quality, we have performed comparisons with the few available measurements. Above about 30 km there is good consistency with observations from ATMOS, the only available information there. In the altitude range between 20 and 30 km to our knowledge there are no observations of the background SO_2 distribution to compare with. At 14–20 km we could compare with measurements of ACE-FTS during the same volcanically enhanced period showing generally smaller values of MIPAS of around 30 %. This might be explained by the different sampling pattern of the two instruments and the different time-period (whole month after the eruption in case of MIPAS vs. half month in case of ACE-FTS). In-situ observations are also sparse above 14 km and not globally available. In general, the MIPAS mid-latitude global mean values at the lower heights (about 10–20 pptv with a standard deviation of about 10 pptv) are within, but at the lower limit of the stratospheric in-situ data with values of roughly 10–50 pptv. Apart from any possible bias of the MIPAS or the in-situ datasets this might stem from differences in the observing altitudes (in-situ mostly below 15 km) or geographic location for higher altitudes (in-situ mostly over northern continents).

ACPD
13, 12389–12436, 2013

A further hint for the validity of our results is the general consistency with the understanding of the behaviour of SO_2 from model results. In this respect we could observe for the first time the local maximum of SO_2 at around 25–30 km resulting from conversion of COS (Brühl et al., 2012). Further, the MIPAS data corroborate the strong increase of SO_2 above 30–35 km explained by photolysis of H_2SO_4 (Rinsland et al., 1995; Vaida et al., 2003; Mills et al., 2005). The observed increase is larger than the one modelled in Brühl et al. (2012) which can be explained by neglect of the visible and near-IR photolysis bands of H_2SO_4 (Vaida et al., 2003; Brühl et al., 2013). The explanation for the fast increase of small aerosol particles at high latitudes in spring as the conversion from SO_2 on availability of sunlight (Mills et al., 2005) can be followed in terms of an annually reoccurring depletion of SO_2 which has been observed for the first time.

The global height-resolved fields of SO_2 in the lower stratosphere over 10 yr confirm the importance of volcanic eruptions for the distribution of sulfate in that region. No other source of SO_2 comparable to that of volcanoes could be detected. This supports the conclusions of e.g. Neely et al. (2013) and Vernier et al. (2011) on the minor importance of an anthropogenic influence. Further, the current dataset will help to test model simulations, based on total SO_2 injection masses from nadir sounders (Neely et al., 2013; Brühl et al., 2013), on the distribution and total mass entry of SO_2 into the stratosphere.

A multivariate regression analysis of the SO_2 time series at different altitude-latitude bins with global coverage revealed a QBO signal at around 30 km in the tropics and a SAO signal above at tropical and sub-tropical latitudes. Further, there appears a possible connection with the solar cycle above 30 km at equatorial and southern mid-latitudes. Significant signals of linear trends are detected at altitudes up to 30 km in the Southern Hemisphere (positive), at high altitude southern mid-latitudes (negative), and at lower tropical altitudes (negative). The negative linear trend at low latitudes is caused by the signal of tropical volcanic eruptions leading to peaks of enhanced SO_2 volume mixing ratios until end of 2006.

In this study we have concentrated on the retrieval from average spectra which enabled us to get SO_2 distributions throughout the stratosphere with a moderate temporal and latitudinal resolution. As shown, these results are e.g. useful for validation of the sulfur budget in chemistry-transport and chemistry-climate models above about 15 km. A direct comparison of such a model with our results is investigated in a parallel study (Brühl et al., 2013). The retrieval from mean spectra is, however, not the optimal way to study the behaviour of SO_2 in the upper troposphere and lowest stratosphere where a resolution in longitudinal direction and a retrieval down to lower altitudes is desirable. Thus, as a complementary approach single-profiles retrievals from MIPAS which will cover the altitude range up to about 20 km are currently in progress. With such a dataset it will e.g. be possible to follow the height-resolved evolution of volcanic plumes.

The retrieval of COS distributions from MIPAS, as investigated initially in Burgess et al. (2005), and the reconstruction of sulfate aerosol properties, as shown in case of MIPAS-Balloon by Echle et al. (1998) will be further significant steps forward to reach an experimentally based closure of the stratospheric sulfur budget under conditions of moderate volcanic influence as observed during the lifetime of Envisat.

Acknowledgements. We acknowledge provision of MIPAS level-1b calibrated spectra by ESA, meteorological data by ECMWF, $F_{10.7}$ cm solar radio flux by the NOAA Space Weather Prediction Center, Singapore time series of winds by the Free University of Berlin and data on volcanic activity by the Smithsonian's Global Volcanism Program and by NASA's Global Sulfur Dioxide Monitoring Home Page. Further we would like to thank Ch. Brühl for helpful discussions. We acknowledge support by Deutsche Forschungsgemeinschaft and Open Access Publishing Fund of Karlsruhe Institute of Technology.

The service charges for this open access publication
have been covered by a Research Centre of the
Helmholtz Association.

References

Belmont, A. D. and Dartt, D. G.: Semiannual variation in zonal wind from 20 to 65 km at 80° N–10° S, J. Geophys. Res., 78, 6373, doi:10.1029/JC078i027p06373, 1973. 12408

Bourassa, A. E., Robock, A., Randel, W. J., Deshler, T., Rieger, L. A., Lloyd, N. D., Llewellyn, E. J., and Degenstein, D. A.: Large volcanic aerosol load in the Stratosphere linked to Asian monsoon transport, Science, 337, 78–81, doi:10.1126/science.1219371, 2012. 12391, 12421

Bourassa, A. E., Robock, A., Randel, W. J., Deshler, T., Rieger, L. A., Lloyd, N. D., Llewellyn, E. J., and Degenstein, D. A.: Response to Comments on "Large Volcanic Aerosol Load in the Stratosphere Linked to Asian Monsoon Transport", Science, 339, 647, doi:10.1126/science.1227961, 2013. 12421

Brühl, C., Lelieveld, J., Crutzen, P. J., and Tost, H.: The role of carbonyl sulphide as a source of stratospheric sulphate aerosol and its impact on climate, Atmos. Chem. Phys., 12, 1239–1253, doi:10.5194/acp-12-1239-2012, 2012. 12391, 12402, 12403, 12411

Brühl, C., Lelieveld, J., Höpfner, M., and Tost, H.: Stratospheric SO_2 and sulphate aerosol, model simulations and satellite observations, Atmos. Chem. Phys. Discuss., 13, 11395–11425, doi:10.5194/acpd-13-11395-2013, 2013. 12403, 12411, 12412

Burgess, A. B., Grainger, R. G., and Dudhia, A.: Progress in the retrieval of sulphur species from MIPAS, in: Envisat ERS Symposium, ESA Special Publication, vol. 572, 2005. 12392, 12412

Carboni, E., Grainger, R., Walker, J., Dudhia, A., and Siddans, R.: A new scheme for sulphur dioxide retrieval from IASI measurements: application to the Eyjafjallajökull eruption of April and May 2010, Atmos. Chem. Phys., 12, 11417–11434, doi:10.5194/acp-12-11417-2012, 2012. 12392

Carn, S. A. and Prata, F. J.: Satellite-based constraints on explosive SO_2 release from Soufrière Hills Volcano, Montserrat, Geophys. Res. Lett., 37, L00E22, doi:10.1029/2010GL044971, 2010. 12421

Clarisse, L., Hurtmans, D., Clerbaux, C., Hadji-Lazaro, J., Ngadi, Y., and Coheur, P.-F.: Retrieval of sulphur dioxide from the infrared atmospheric sounding interferometer (IASI), Atmos. Meas. Tech., 5, 581–594, doi:10.5194/amt-5-581-2012, 2012. 12421

Cole, P., Bass, V., Christopher, C., Fergus, M., Gunn, L., Odbert, H., Simpson, R., Stewart, R., Stinton, A., Stone, J., Syers, R., Robertson, R., Watts, R., and Williams, P.: Report to the

Scientific Advisory Committee on Montserrat Volcanic Activity, Report on Activity between 15 August 2009 and 28 February 2010, Tech. rep., Montserrat Volcano Observatory, open File Report OFR 10-01a, 2010. 12421

Crutzen, P. J.: The possible importance of CSO for the sulfate layer of the stratosphere, Geophys. Res. Lett., 3, 73–76, doi:10.1029/GL003i002p00073, 1976. 12391, 12402

Delisi, D. P. and Dunkerton, T. J.: Seasonal variation of the semiannual oscillation., J. Atmos. Sci., 45, 2772–2809, doi:10.1175/1520-0469(1988)045<2772:SVOTSO>2.0.CO;2, 1988. 12408

Deshler, T., Anderson-Sprecher, R., Jäger, H., Barnes, J., Hofmann, D. J., Clemesha, B., Simonich, D., Osborn, M., Grainger, R. G., and Godin-Beekmann, S.: Trends in the nonvolcanic component of stratospheric aerosol over the period 1971–2004, J. Geophys. Res., 111, D01201, doi:10.1029/2005JD006089, 2006. 12391

Doeringer, D., Eldering, A., Boone, C. D., González Abad, G., and Bernath, P. F.: Observation of sulfate aerosols and SO_2 from the Sarychev volcanic eruption using data from the Atmospheric Chemistry Experiment (ACE), J. Geophys. Res., 117, D03203, doi:10.1029/2011JD016556, 2012. 12392, 12395, 12399, 12400, 12405

Echle, G., von Clarmann, T., and Oelhaf, H.: Optical and microphysical parameters of the Mt. Pinatubo aerosol as determined from MIPAS–B mid–IR limb emission spectra, J. Geophys. Res., 103, 19193–19211, doi:10.1029/98JD01363, 1998. 12412

Fischer, H., Birk, M., Blom, C., Carli, B., Carlotti, M., von Clarmann, T., Delbouille, L., Dudhia, A., Ehhalt, D., Endemann, M., Flaud, J. M., Gessner, R., Kleinert, A., Koopman, R., Langen, J., López-Puertas, M., Mosner, P., Nett, H., Oelhaf, H., Perron, G., Remedios, J., Ridolfi, M., Stiller, G., and Zander, R.: MIPAS: an instrument for atmospheric and climate research, Atmos. Chem. Phys., 8, 2151–2188, doi:10.5194/acp-8-2151-2008, 2008. 12393

Fromm, M., Nedoluha, G., and Charvát, Z.: Comment on "Large Volcanic Aerosol Load in the Stratosphere Linked to Asian Monsoon Transport", Science, 339, 647, doi:10.1126/science.1228605, 2013. 12421

Garcia, R. R., Dunkerton, T. J., Lieberman, R. S., and Vincent, R. A.: Climatology of the semiannual oscillation of the tropical middle atmosphere, J. Geophys. Res., 102, 26019–26032, doi:10.1029/97JD00207, 1997. 12408

Hofmann, D., Barnes, J., O'Neill, M., Trudeau, M., and Neely, R.: Increase in background stratospheric aerosol observed with lidar at Mauna Loa Observatory and Boulder, Colorado, Geophys. Res. Lett., 36, L15808, doi:10.1029/2009GL039008, 2009. 12391

ACPD
13, 12389–12436, 2013

Title Page
Abstract | Introduction
Conclusions | References
Tables | Figures
Back | Close
Full Screen / Esc
Printer-friendly Version
Interactive Discussion

Hofmann, D. J.: Measurement of the condensation nuclei profile to 31 km in the Arctic in January 1989 and comparisons with Antarctic measurements, Geophys. Res. Lett., 17, 357–360, doi:10.1029/GL017i004p00357, 1990. 12391
Hofmann, D. J. and Rosen, J. M.: Antarctic observations of stratospheric aerosol and high altitude condensation nuclei following the El Chichon eruption, Geophys. Res. Lett., 12, 13–16, doi:10.1029/GL012i001p00013, 1985. 12391
Höpfner, M., Orphal, J., von Clarmann, T., Stiller, G., and Fischer, H.: Stratospheric $BrONO_2$ observed by MIPAS, Atmos. Chem. Phys., 9, 1735–1746, doi:10.5194/acp-9-1735-2009, 2009a. 12394, 12397
Höpfner, M., Pitts, M. C., and Poole, L. R.: Comparison between CALIPSO and MIPAS observations of polar stratospheric clouds, J. Geophys. Res., 114, D00H05, doi:10.1029/2009JD012114, 2009b. 12394
Inn, E. C. Y. and Vedder, J. F.: Measurements of stratospheric sulfur constituents, Geophys. Res. Lett., 8, 5–8, 1981. 12400, 12420
Jaeschke, W., Georgii, H.-W., and Schmitt, R.: Preliminary results of stratospheric SO_2 measurements, Geophys. Res. Lett., 3, 517–519, 1976. 12400, 12420
Jurkat, T., Voigt, C., Arnold, F., Schlager, H., Aufmhoff, H., Schmale, J., Schneider, J., Lichtenstern, M., and Dörnbrack, A.: Airborne stratospheric ITCIMS measurements of SO_2, HCl, and HNO_3 in the aged plume of volcano Kasatochi, J. Geophys. Res., 115, D00L17, doi:10.1029/2010JD013890, 2010. 12420
Kiefer, M., von Clarmann, T., Grabowski, U., De Laurentis, M., Mantovani, R., Milz, M., and Ridolfi, M.: Characterization of MIPAS elevation pointing, Atmos. Chem. Phys., 7, 1615–1628, doi:10.5194/acp-7-1615-2007, 2007. 12397
Kyrölä, E., Tamminen, J., Sofieva, V., Bertaux, J. L., Hauchecorne, A., Dalaudier, F., Fussen, D., Vanhellemont, F., Fanton d'Andon, O., Barrot, G., Guirlet, M., Fehr, T., and Saavedra de Miguel, L.: GOMOS O_3, NO_2, and NO_3 observations in 2002–2008, Atmos. Chem. Phys., 10, 7723–7738, doi:10.5194/acp-10-7723-2010, 2010. 12406, 12407
Meixner, F. X.: The vertical sulfur dioxide distribution at the tropopause level, J. Atmos. Chem., 2, 175–189, 1984. 12400, 12420
Mills, M. J., Toon, O. B., and Solomon, S.: A 2D microphysical model of the polar stratospheric CN layer, Geophys. Res. Lett., 26, 1133–1136, doi:10.1029/1999GL900187, 1999. 12391
Mills, M. J., Toon, O. B., Vaida, V., Hintze, P. E., Kjaergaard, H. G., Schofield, D. P., and Robinson, T. W.: Photolysis of sulfuric acid vapor by visible light as a source of the polar

stratospheric CN layer, J. Geophys. Res., 110, D08201, doi:10.1029/2004JD005519, 2005. 12391, 12403, 12404, 12411

Möhler, O. and Arnold, F.: Gaseous sulfuric acid and sulfur dioxide measurements in the Arctic troposphere and lower stratosphere: implications for hydroxyl radical abundances, Geophys. Res. Lett., 19, 1763–1766, 1992. 12420

Neely, R. R., Toon, O. B., Solomon, S., Vernier, J. P., Alvarez, C., English, J. M., Rosenlof, K. H., Mills, M. J., Bardeen, C. G., Daniel, J. S., and Thayer, J. P.: Recent anthropogenic increases in SO_2 from Asia have minimal impact on stratospheric aerosol, Geophys. Res. Lett., 40, 999–1004, doi:10.1002/grl.50263, 2013. 12404, 12411, 12421

Piccolo, C. and Dudhia, A.: Precision validation of MIPAS-Envisat products, Atmos. Chem. Phys., 7, 1915–1923, doi:10.5194/acp-7-1915-2007, 2007. 12401

Ray, E. A., Alexander, M. J., and Holton, J. R.: An analysis of the structure and forcing of the equatorial semiannual oscillation in zonal wind, J. Geophys. Res., 103, 1759–1774, doi:10.1029/97JD02679, 1998. 12408

Read, W. G., Froidevaux, L., and Waters, J. W.: Microwave limb sounder measurement of stratospheric SO_2 from the Mount Pinatubo volcano, Geophys. Res. Lett., 20, 1299–1302, doi:10.1029/93GL00831, 1993. 12392

Rinsland, C. P., Gunson, M. R., Ko, M. K. W., Weisenstein, D. W., Zander, R., Abrams, M. C., Goldman, A., Sze, N. D., and Yue, G. K.: H_2SO_4 photolysis: a source of sulfur dioxide in the upper stratosphere, Geophys. Res. Lett., 22, 1109–1112, doi:10.1029/95GL00917, 1995. 12391, 12392, 12395, 12398, 12399, 12411, 12429

Rodgers, C. D.: Inverse Methods for Atmospheric Sounding: Theory and Practice, vol. 2, edited by: Taylor, F. W., Series on Atmospheric, Oceanic and Planetary Physics, World Scientific, 2000. 12395

Rosen, J. M. and Hofmann, D. J.: Unusual behavior in the condensation nuclei concentration at 30 km, J. Geophys. Res., 88, 3725–3731, doi:10.1029/JC088iC06p03725, 1983. 12391

Rothman, L. S., Gordon, I. E., Barbe, A., Benner, D. C., Bernath, P. F., Birk, M., Boudon, V., Brown, L. R., Campargue, A., Champion, J.-P., Chance, K., Coudert, L. H., Dana, V., Devi, V. M., Fally, S., Flaud, J.-M., Gamache, R. R., Goldman, A., Jacquemart, D., Kleiner, I., Lacome, N., Lafferty, W. J., Mandin, J.-Y., Massie, S. T., Mikhailenko, S. N., Miller, C. E., Moazzen-Ahmadi, N., Naumenko, O. V., Nikitin, A. V., Orphal, J., Perevalov, V. I., Perrin, A., Predoi-Cross, A., Rinsland, C. P., Rotger, M., Šimečková, M., Smith, M. A. H., Sung, K., Tashkun, S. A., Tennyson, J., Toth, R. A., Vandaele, A. C., and Vander Auwera, J.: The

ACPD
13, 12389–12436, 2013

Stratospheric SO_2 by MIPAS

M. Höpfner et al.

HITRAN 2008 molecular spectroscopic database, J. Quant. Spectrosc. Ra., 110, 533–572, doi:10.1016/j.jqsrt.2009.02.013, 2009. 12395, 12397

Solomon, S., Daniel, J. S., Neely, R. R., Vernier, J.-P., Dutton, E. G., and Thomason, L. W.: The persistently variable "Background" stratospheric aerosol layer and global climate change, Science, 333, 866–870, doi:10.1126/science.1206027, 2011. 12391

Spang, R., Remedios, J. J., and Barkley, M. P.: Colour indices for the detection and differentiation of cloud types in infra-red limb emission spectra, Adv. Space Res., 33, 1041–1047, 2004. 12394

SPARC: Assessment of Stratospheric Aerosol Properties (ASAP), SPARC Report No. 4, WCRP-124, WMO/TD-No. 1295, February 2006, edited by: Thomason, L. and Peter, T., 2006. 12391, 12392, 12399, 12403

Steck, T.: Methods for determining regularization for atmospheric retrieval problems, Appl. Opt., 41, 1788–1797, 2002. 12395

Stiller, G. P.: The Karlsruhe Optimized and Precise Radiative Transfer Algorithm (KOPRA), vol. FZKA 6487, Wissenschaftliche Berichte, Forschungszentrum Karlsruhe, 2000. 12395

Stiller, G. P., von Clarmann, T., Haenel, F., Funke, B., Glatthor, N., Grabowski, U., Kellmann, S., Kiefer, M., Linden, A., Lossow, S., and López-Puertas, M.: Observed temporal evolution of global mean age of stratospheric air for the 2002 to 2010 period, Atmos. Chem. Phys., 12, 3311–3331, doi:10.5194/acp-12-3311-2012, 2012. 12406, 12408

Surono, Jousset, P., Pallister, J., Boichu, M., Buongiorno, M. F., Budisantoso, A., Costa, F., Andreastuti, S., Prata, F., Schneider, D., Clarisse, L., Humaida, H., Sumarti, S., Bignami, C., Griswold, J., Carn, S., Oppenheimer, C., and Lavigne, F.: The 2010 explosive eruption of Java's Merapi volcano – A "100-year" event, J. Volcanol. Geoth. Res., 241, 121–135, doi:10.1016/j.jvolgeores.2012.06.018, 2012. 12421

Theys, N., Campion, R., Clarisse, L., Brenot, H., van Gent, J., Dils, B., Corradini, S., Merucci, L., Coheur, P.-F., Van Roozendael, M., Hurtmans, D., Clerbaux, C., Tait, S., and Ferrucci, F.: Volcanic SO_2 fluxes derived from satellite data: a survey using OMI, GOME-2, IASI and MODIS, Atmos. Chem. Phys. Discuss., 12, 31349–31412, doi:10.5194/acpd-12-31349-2012, 2012. 12391

Thornton, D. C., Bandy, A. R., Blomquist, B. W., Driedger, A. R., and Wade, T. P.: Sulfur dioxide distribution over the Pacific Ocean 1991–1996, J. Geophys. Res., 104, 5845–5854, 1999. 12420

ACPD

13, 12389–12436, 2013

Stratospheric SO_2 by MIPAS

M. Höpfner et al.

Tikhonov, A.: On the solution of incorrectly stated problems and method of regularization, Dokl. Akad. Nauk. SSSR, 151, 501–504, 1963. 12395

Trepte, C. R. and Hitchman, M. H.: Tropical stratospheric circulation deduced from satellite aerosol data, Nature, 355, 626–628, doi:10.1038/355626a0, 1992. 12407

Vaida, V., Kjaergaard, H. G., Hintze, P. E., and Donaldson, D. J.: Photolysis of sulfuric acid vapor by visible solar radiation, Science, 299, 1566–1568, doi:10.1126/science.1079297, 2003. 12391, 12403, 12411

Van Gent, J., Spurr, R., Lerot, C., Van Roozendael, M., Theys, N., and Brenot, H.: SO_2 plume height retrieval from direct fitting of GOME-2 backscattered radiance measurements, in: 39th COSPAR Scientific Assembly, 14–22 July 2012, Mysore, India, Abstract C0.3-1-12, p.2048, vol. 39, COSPAR Meeting, 2012. 12391

Vernier, J.-P., Thomason, L. W., Pommereau, J.-P., Bourassa, A., Pelon, J., Garnier, A., Hauchecorne, A., Blanot, L., Trepte, C., Degenstein, D., and Vargas, F.: Major influence of tropical volcanic eruptions on the stratospheric aerosol layer during the last decade, Geophys. Res. Lett., 38, L12807, doi:10.1029/2011GL047563, 2011. 12391, 12406, 12407, 12411

Vernier, J.-P., Thomason, L. W., Fairlie, T. D., Minnis, P., Palikonda, R., and Bedka, K. M.: Comment on "Large Volcanic Aerosol Load in the Stratosphere Linked to Asian Monsoon Transport", Science, 339, 647, doi:10.1126/science.1227817, 2013. 12421

von Clarmann, T., Ceccherini, S., Doicu, A., Dudhia, A., Funke, B., Grabowski, U., Hilgers, S., Jay, V., Linden, A., López-Puertas, M., Martín-Torres, F.-J., Payne, V., Reburn, J., Ridolfi, M., Schreier, F., Schwarz, G., Siddans, R., and Steck, T.: A blind test retrieval experiment for infrared limb emission spectrometry, J. Geophys. Res., 108, 4746, doi:10.1029/2003JD003835, 2003a. 12395

von Clarmann, T., Glatthor, N., Grabowski, U., Höpfner, M., Kellmann, S., Kiefer, M., Linden, A., Mengistu Tsidu, G., Milz, M., Steck, T., Stiller, G. P., Wang, D. Y., Fischer, H., Funke, B., Gil-López, S., and López-Puertas, M.: Retrieval of temperature and tangent altitude pointing from limb emission spectra recorded from space by the Michelson Interferometer for Passive Atmospheric Sounding (MIPAS), J. Geophys. Res., 108, 4736, doi:10.1029/2003JD003602, 2003b. 12397

von Clarmann, T., Höpfner, M., Kellmann, S., Linden, A., Chauhan, S., Funke, B., Grabowski, U., Glatthor, N., Kiefer, M., Schieferdecker, T., Stiller, G. P., and Versick, S.: Retrieval of temperature, H_2O, O_3, HNO_3, CH_4, N_2O, $ClONO_2$ and ClO from MIPAS reduced resolution nominal

ACPD
13, 12389–12436, 2013

Stratospheric SO_2 by MIPAS

M. Höpfner et al.

mode limb emission measurements, Atmos. Meas. Tech., 2, 159–175, doi:10.5194/amt-2-159-2009, 2009. 12397

von Clarmann, T., Stiller, G., Grabowski, U., Eckert, E., and Orphal, J.: Technical Note: Trend estimation from irregularly sampled, correlated data, Atmos. Chem. Phys., 10, 6737–6747, doi:10.5194/acp-10-6737-2010, 2010. 12406

Wilson, J. C., Stolzenburg, M. R., Clark, W. E., Loewenstein, M., Ferry, G. V., and Chan, K. R.: Measurements of condensation nuclei in the airborne arctic stratospheric expedition – observations of particle production in the polar vortex, Geophys. Res. Lett., 17, 361–364, doi:10.1029/GL017i004p00361, 1990. 12391

Zhao, J., Toon, O. B., and Turco, R. P.: Origin of condensation nuclei in the springtime polar stratosphere, J. Geophys. Res., 100, 5215–5227, doi:10.1029/94JD03110, 1995. 12391

ACPD
13, 12389–12436, 2013

Stratospheric SO_2 by MIPAS

M. Höpfner et al.

Table 1. In-situ observations of SO_2 in the lower stratosphere.

Ref.	Date	Location	Altitude [km]	VMR pptv
Jaeschke et al. (1976)	Spring 1976	54° N	14	52
Inn and Vedder (1981)	Jun–Jul 1979	38,64,67° N	15.2–20.4	36–51
Meixner (1984)	1978–80	50° N (W-Europe)	10.7–15.2	Dec: 8–33 Apr/May: 13–41(115) Sep: 25–46
Möhler and Arnold (1992)	Feb 1987	67° N (N-Europe)	tropopause tropopause+2.5 km	100 10
Thornton et al. (1999)	1991–1996	W-Pacific	12	60
Jurkat et al. (2010)	Oct 2008	Europe	11.5	20–55 (strat background) 510 (Kasatochi)

ACPD
13, 12389–12436, 2013

Stratospheric SO_2 by MIPAS

M. Höpfner et al.

Table 2. Major volcanic eruptions in the time period of the MIPAS measurements. General data of volcanoes are from http://www.volcano.si.edu. Injection heights and SO_2 masses are based on Neely et al. (2013, Table S1) and references therein. References for additional eruptions: Soufrière Hills on 12 July 2003: Carn and Prata (2010), Soufrière Hills on 11 February 2010: Cole et al. (2010), Nabro mass: Clarisse et al. (2012), Nabro injection height: Bourassa et al. (2012) and connected discussion (Fromm et al., 2013; Vernier et al., 2013; Bourassa et al., 2013), Merapi: Surono et al. (2012). In case of Pacaya, the SO_2 mass is taken from Aura/OMI measurements on 30 May 2010 (http://so2.gsfc.nasa.gov).

Name	Location	Eruption date	SO_2 mass [Tg]	Injection height [km]
Ruang	2.3° N, 125.4° E	25 Sep 2002	0.055	20
El Reventador	0.1° S, 77.7° W	3 Nov 2002	0.096	17
Soufrière Hills	16.7° N, 62.2° W	12 Jul 2003	0.12	15
Anatahan	16.4° N, 145.7° E	12 Apr 2004	0.065	15
Manam	4.1° S, 145° E	27 Jan 2005	0.18	19
Sierra Negra	0.8° S, 91.2° W	22 Oct 2005	0.36	15
Soufrière Hills	16.7° N, 62.2° W	20 May 2006	0.2	20
Rabaul (Tavurvur)	4.3° S, 152.2° E	7 Oct 2006	0.125	17
Tair, Jebel al	15.5° N, 41.8° E	30 Sep 2007	0.08	16
Chaiten	42.8° S, 72.6° W	2 May 2008	0.01	19
Okmok	53.4° N, 168.1° W	12 Jul 2008	0.122	16
Kasatochi	52.2° N, 175.5° W	7 Aug 2008	1.7	14–18
Sarychev	48.1° N, 153.2° E	12 Jun 2009	1.4	17
Soufrière Hills	16.7° N, 62.2° W	11 Feb 2010	0.05	15
Pacaya	14.4° N, 90.6° W	28 May 2010	0.02	
Merapi	7.5° S, 110.4° E	26 Oct 2010	0.44	17
Nabro	13.4° N, 41.7° E	12 Jun 2011	1.5	14–16

ACPD
13, 12389–12436, 2013

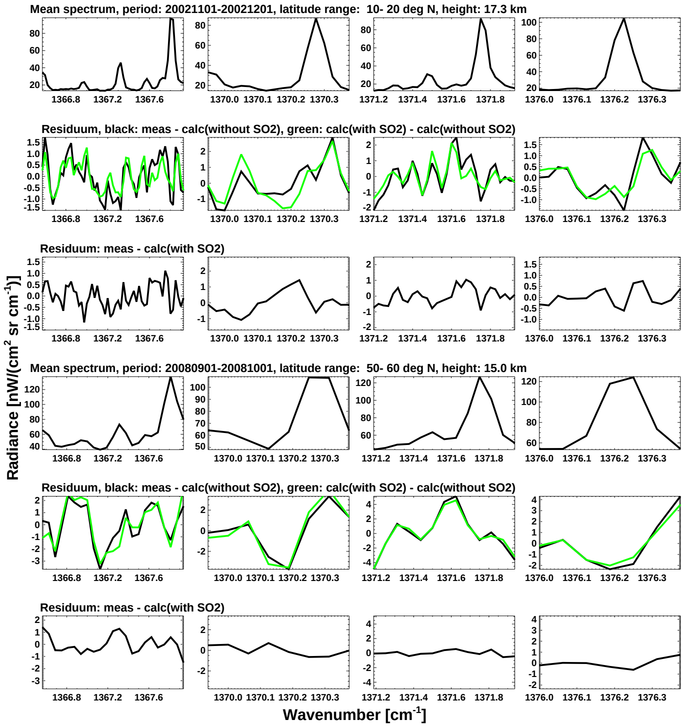

Fig. 1. Spectral identification and fit quality of the SO_2 retrieval. The columns show the four spectral windows used. The top three rows refer to the first observational period (P1) while rows 4–6 belong to the second period with lower spectral resolution (P2). Rows 1 and 4 contain the measured spectra. The black curves in the panels of row 2 and 5 show the residua after the spectral fit when no SO_2 is considered and the black curves in the 3rd and 6th row are the residua in case SO_2 is added as a fitting parameter. The green curves in row 2 and 5 indicate the spectral features of SO_2 based on simulations only.

ACPD
13, 12389–12436, 2013

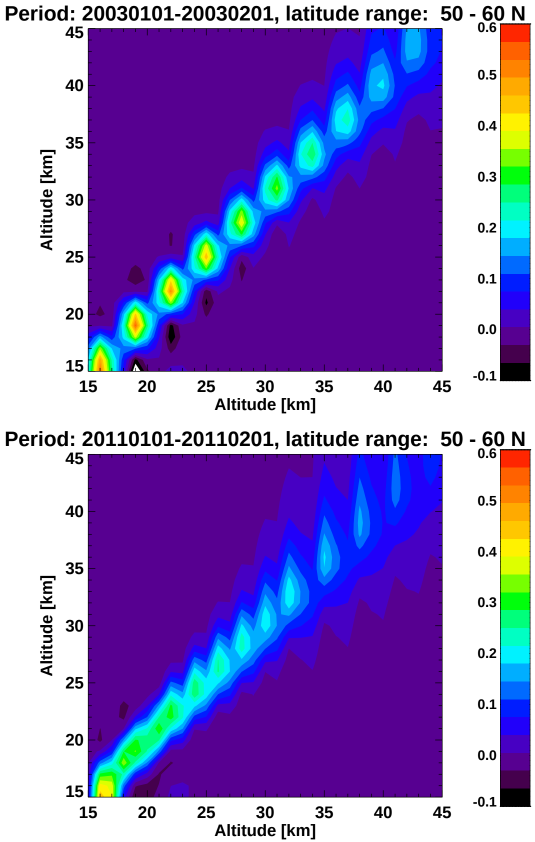

Fig. 2. Example of averaging kernels for SO_2 at mid-latitudes within the first (top) and the second (bottom) MIPAS measurement period.

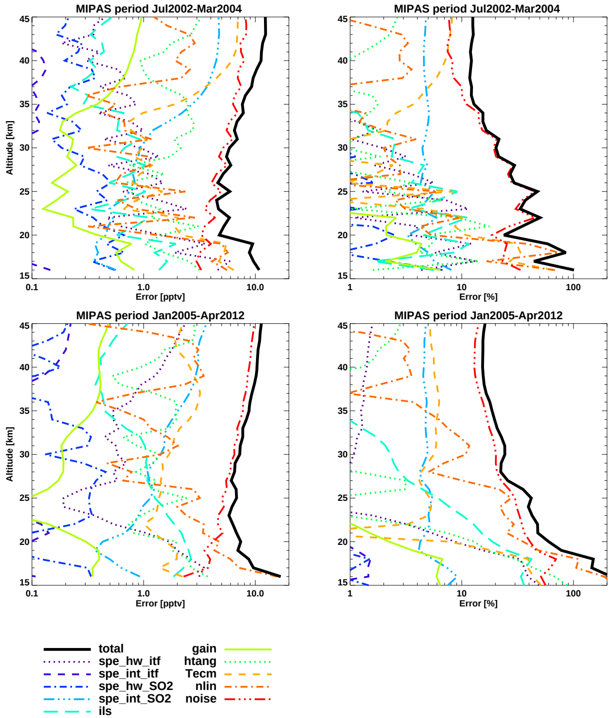

Fig. 3. Error estimation of the retrieval for one month during P1 and one month during P2. Considered error sources are the uncertainty of the foreign-broadened half-width and line-intensity of interfering species (spe_hw_itf, spe_int_itf), the knowledge of these parameters for SO_2 (spe_hw_SO2, spe_int_SO2), the uncertainties of the instrumental line-shape and gain-calibration (ils, gain), the errors in the assumed tangent altitudes and temperatures (htang, Tecm), the error due to the applied technique of retrievals from averaged spectra (nlin) and the spectral noise of the instrument (noise). The total error has been determined by quadratic combination of the single error components.

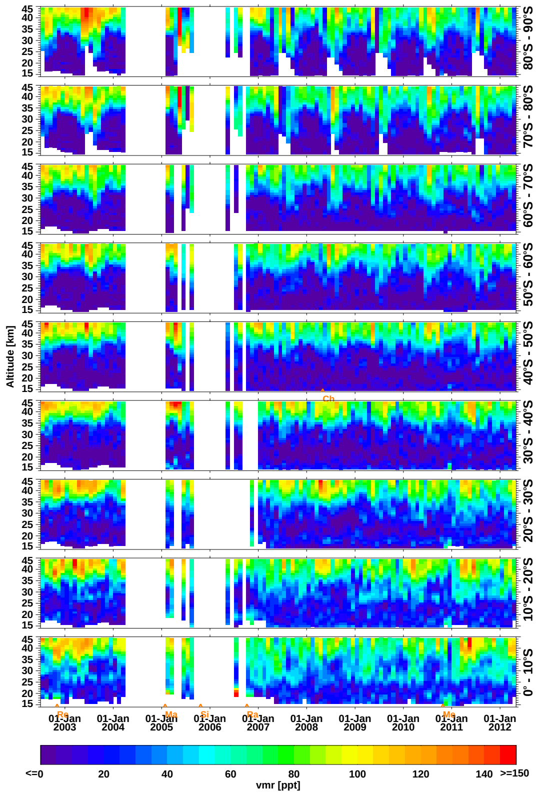

Fig. 4. Time series of color-coded SO_2 monthly mean volume mixing ratio profiles for 10° latitude bins in the Southern Hemisphere. The color scale is restricted to 0–150 pptv: negative and values larger than 150 pptv are given the color belonging to 0 and 150 pptv, respectively. Major volcanic eruptions are indicated within the latitude bin of their location (see Table 2).

ACPD
13, 12389–12436, 2013

Stratospheric SO_2 by MIPAS

M. Höpfner et al.

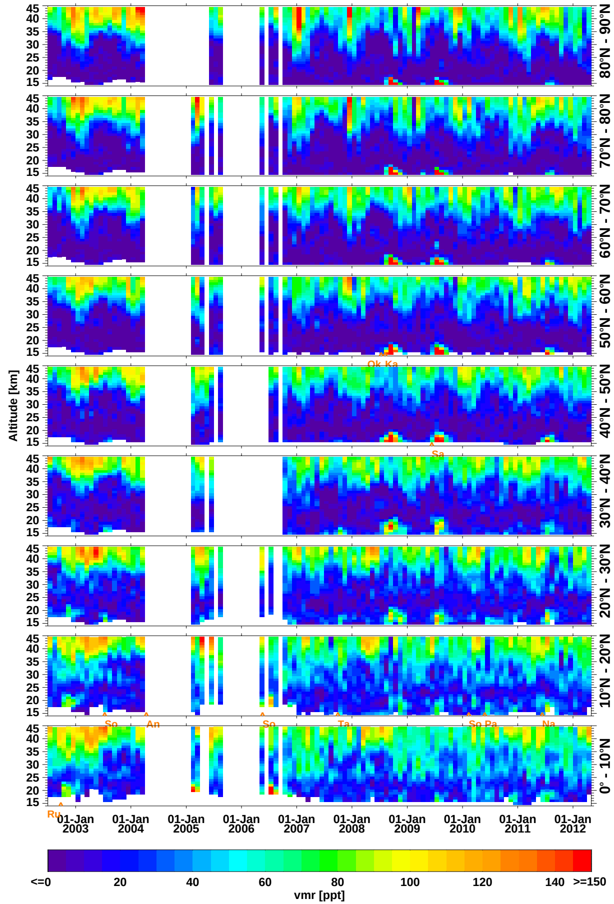

Fig. 5. Same as Fig. 4 but for the Northern Hemisphere.

ACPD
13, 12389–12436, 2013

Stratospheric SO_2 by MIPAS

M. Höpfner et al.

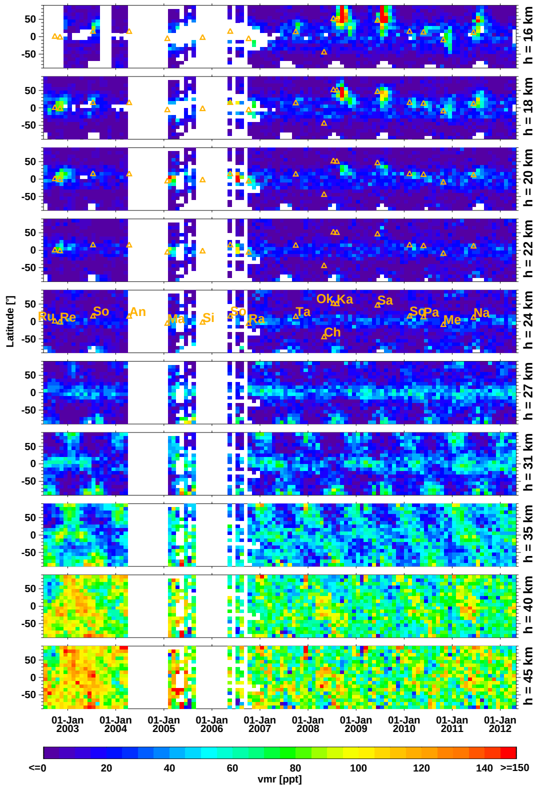

Fig. 6. Global time series of color-coded SO_2 monthly mean distributions at various altitudes. The color scale is restricted to 0–150 pptv: negative and values larger than 150 pptv are given the color belonging to 0 and 150 pptv, respectively. Major volcanic eruptions are indicated by the latitude of their location (Table 2).

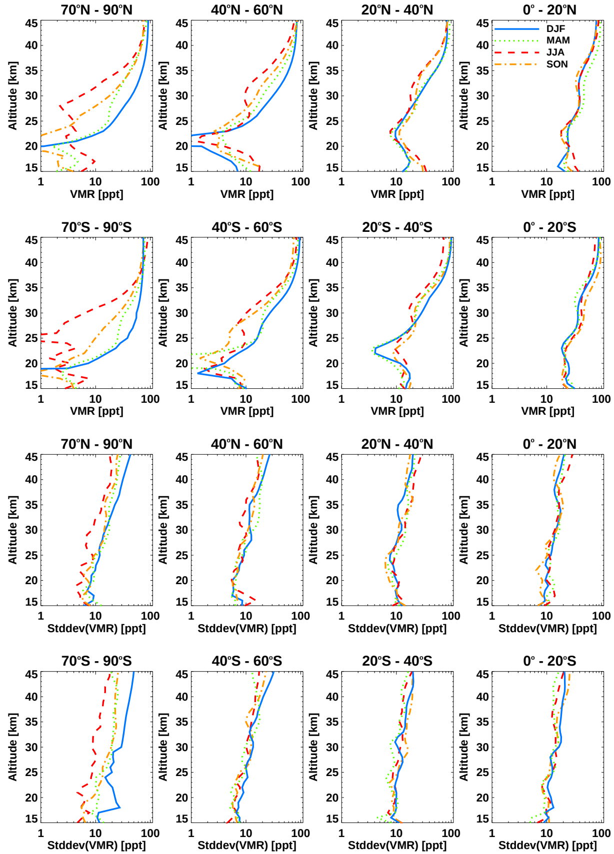

Fig. 7. Mean background seasonal profiles of SO_2 (top two rows) and standard deviation of the distribution (bottom two rows). Periods of major volcanic influence which have been excluded here are: October–December 2002, July 2003, January–June 2005, May–November 2006, October 2007, July–December 2008, June–December 2009, November–December 2010, July–September 2011.

ACPD
13, 12389–12436, 2013

Stratospheric SO_2 by MIPAS

M. Höpfner et al.

ACPD

13, 12389–12436, 2013

Stratospheric SO_2 by MIPAS

M. Höpfner et al.

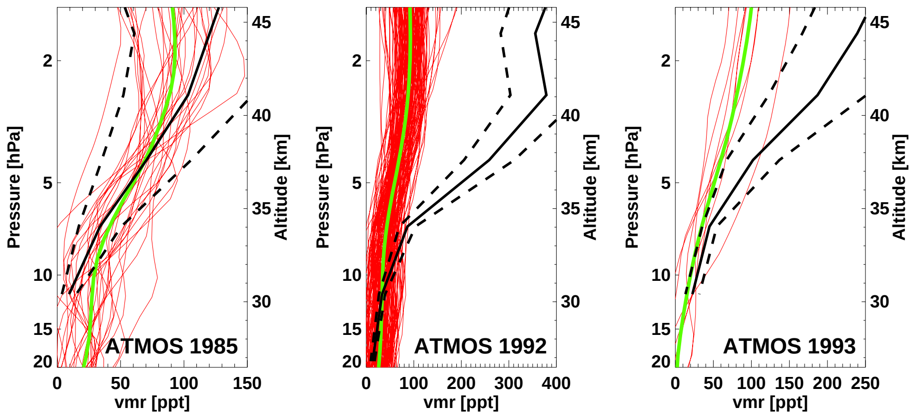

Fig. 8. Comparison of MIPAS observations (2003–2012) of SO_2 (red: single, green: mean) with profiles derived from the ATMOS instrument (black) (Rinsland et al., 1995). Left: SPACELAB 3, April–May 1985, 26° N–32° N vs. MIPAS, April–May 20° N–40° N. Middle: ATLAS 1, March–April 1992, 54° S–28° N vs. MIPAS, March–April 60° S–30°N. Right: ATLAS 2, April 1993, 51° S–44° S vs. MIPAS, April 50° S–40° S.

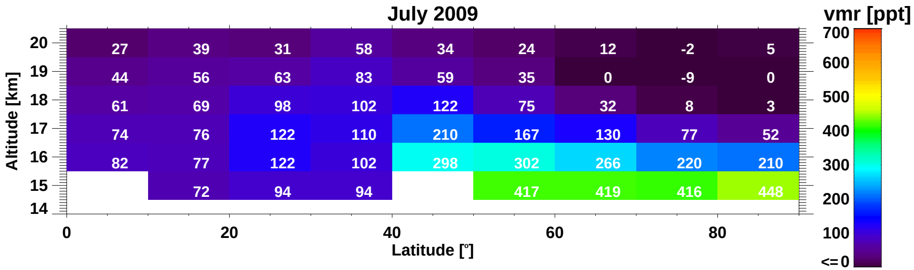

Fig. 9. Latitude-height cross-section of MIPAS zonal mean SO_2 volume mixing ratios in July 2009. Numbers in white show the exact vmr values of each bin in units of ppt.

ACPD
13, 12389–12436, 2013

Stratospheric SO_2 by MIPAS

M. Höpfner et al.

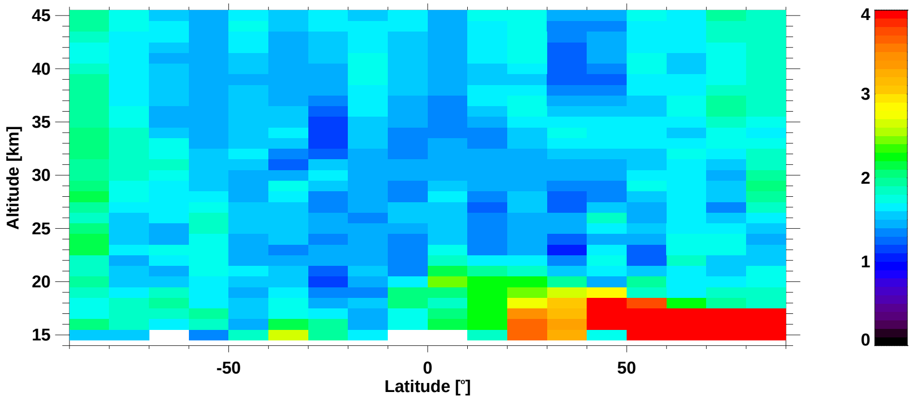

Fig. 10. Global distribution of $\Delta\delta_{l,h}$ as defined in Eq. (3).

ACPD
13, 12389–12436, 2013

Stratospheric SO_2 by MIPAS

M. Höpfner et al.

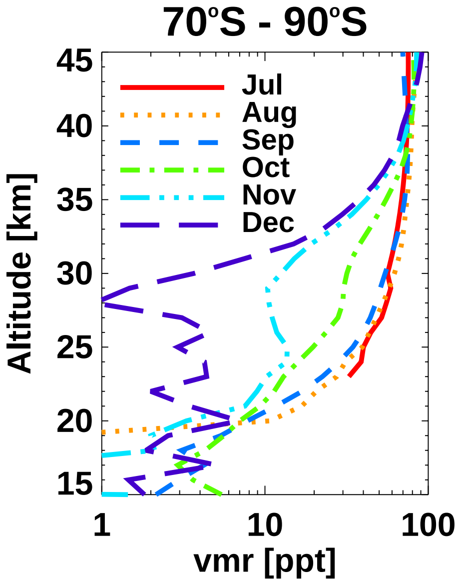

Fig. 11. Temporal evolution of mean Antarctic SO_2 vmr profiles in winter and spring indicating the strong downward transport in winter and subsequent depletion on availability of sunlight.

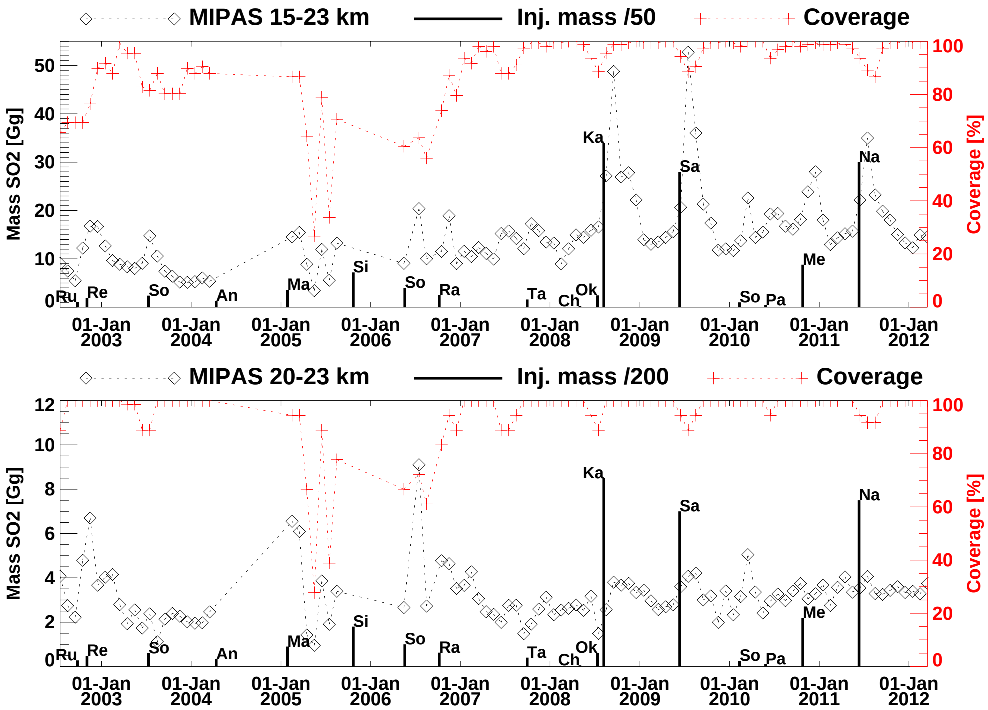

Fig. 12. Black diamonds: global monthly mean SO_2 mass between 15 and 23 km (top) and 20–23 km (bottom) from MIPAS. Black bars: SO_2 injection mass from Table 2. Red: relative coverage of the latitude-height slice with MIPAS observations.

ACPD
13, 12389–12436, 2013

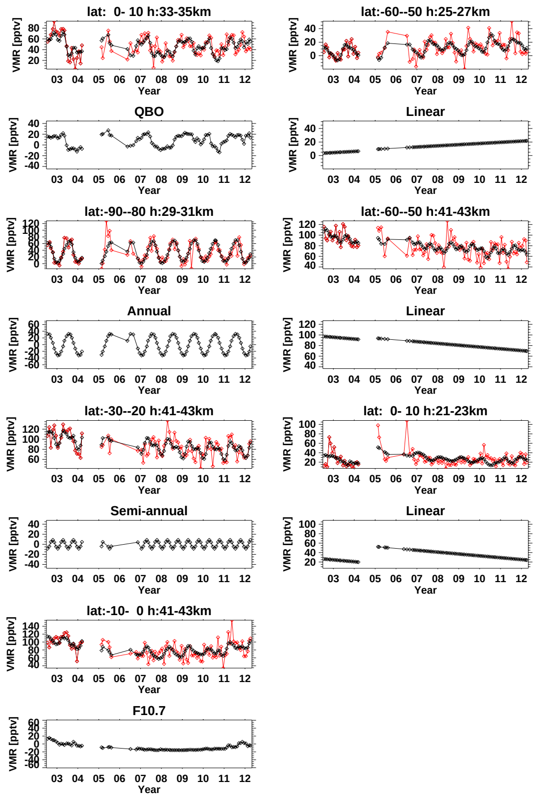

Fig. 13. Time series of multivariate fit results illustrating prominent parameters at different latitude/height regions. Tick marks at the x-axes indicate 1 January of each year. For each parameter two plots are grouped together: the upper one containing the measured dataset in red and the fit in black for the region as specified in the title; the lower plot illustrates the separate weight of the dedicated parameter listed in the title. Left, rows 1 and 2: linear combination of Singapore winds at 10 and 50 hPa; left, rows 3 and 4: annual variation; left, rows 5 and 6: semi-annual variation; left, rows 7 and 8: solar $F_{10.7}$ flux; right column: linear trend and bias.

ACPD
13, 12389–12436, 2013

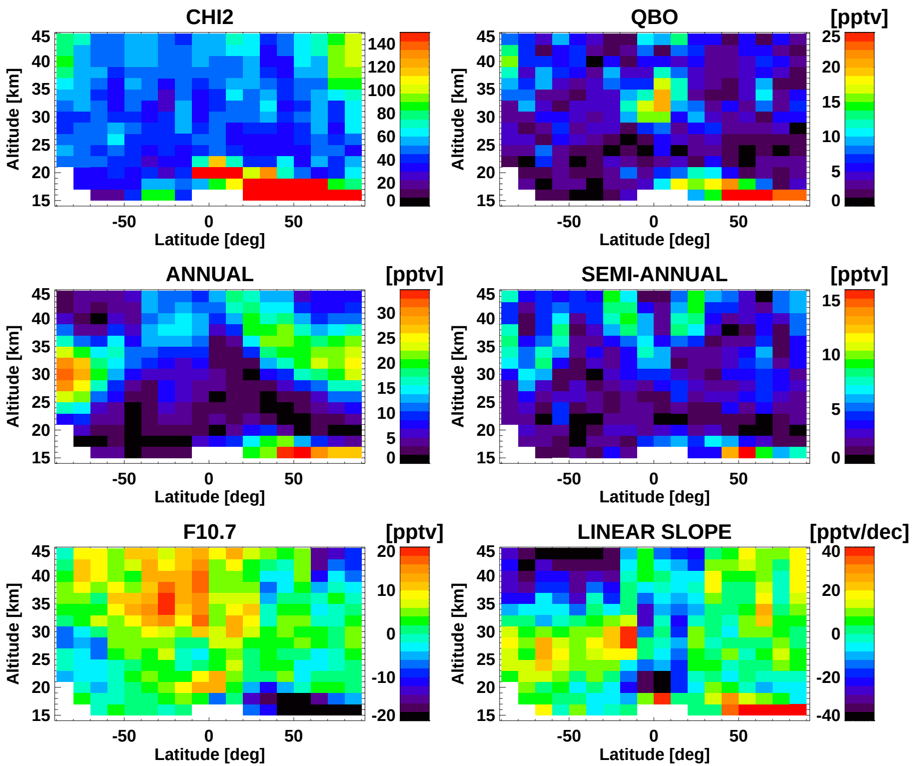

Fig. 14. Global overview of the fit RMS (top left), the amplitudes of various fit parameters and the linear trends (bottom right). For "QBO" and "$F_{10.7}$", the amplitude is defined as the semi-difference between maximum and minimum of the fitted time series of Singapore winds and solar $F_{10.7}$ flux, respectively. For "$F_{10.7}$" the sign indicates a positive or negative correlation with the solar cycle.

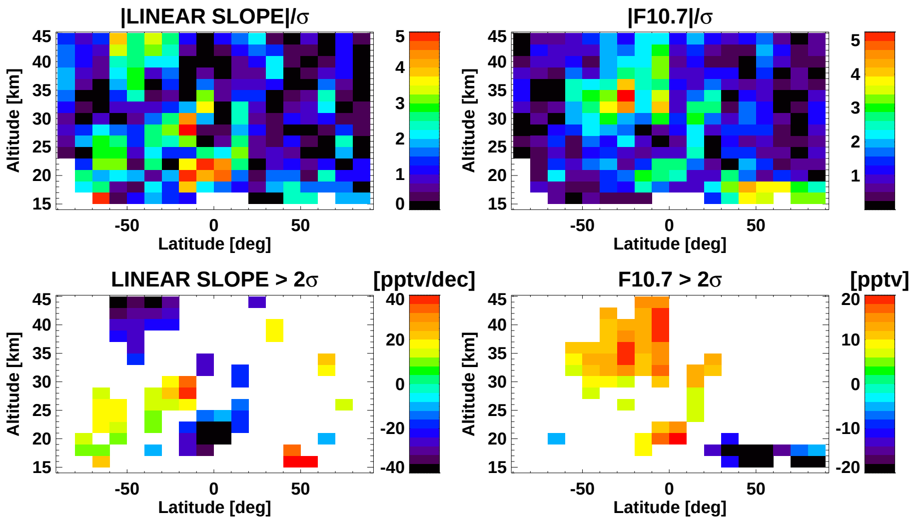

Fig. 15. Top: significance in multiples of the estimated error of the model error corrected linear slope (left) and the $F_{10.7}$ amplitude (see caption of Fig. 14 for definition) (right). Bottom: remaining values with a significance $> 2\sigma$.

ACPD
13, 12389–12436, 2013

Stratospheric SO_2 by MIPAS

M. Höpfner et al.